CrossMark

BRIEF NOTE

Uniaxial strength and failure in sandstone containing a pre-existing 3-D surface flaw

Yinlong Lu · Lianguo Wang · Derek Elsworth

Abstract A series of uniaxial compression experiments were performed on specimens of sandstone containing a pre-existing 3-D surface flaw in various configurations. The influence of the single flaw geometry on the stress–strain response and failure process was recorded and then analyzed in detail including real-time capture of surface cracking process by photographic monitoring. Uniaxial compressive strength drops of 25.7, 33.2 and 21.6 % were observed due to an increase in the flaw length ($2a = 20$–50 mm) and flaw depth ($d = 4$–20 mm) but a decrease in the inclination of the flaw ($\alpha = 75°$–$15°$). The generation of three typical surface cracking patterns, *namely* wing cracks, anti-wing cracks and far-field cracks were identified and these depend on the geometry of the pre-existing surface flaw. Wing cracks initiate more readily from longer pre-existing flaws and those of deeper flaw depth or shallower flaw inclination while anti-wing cracks develop in the converse situation. Impor-

tantly, the stress required for crack initiation appears to decrease with an increase in flaw depth or a decrease in the flaw inclination. Finally, post-test imaging by X-ray computerized tomography defines the form of internal crack patterns including petal and wing cracks and their interaction and defines the macroscopic ultimate failure modes of the specimens and their dependency on the geometry of the pre-existing flaws. Although specimens containing a penetrating 2-D flaw normally rupture in a tensile splitting mode, those with a non-penetrating 3-D flaw generally fail in a combined shear mode which shows an increased dependency on the petal crack as flaw depth increases.

1 Introduction

Crustal rocks are complex heterogeneous aggregates that contain pre-existing flaws at a variety of different scales in the form of cracks, fissures, joints and macro-faults. The deformation and failure behaviors of the rocks are largely dependent on the process of initiation, propagation and coalescence of new cracks from these pre-existing flaws (Horii and Nematnasser 1986; Peng and Johnson 1972). Therefore, an adequate understanding of the mechanisms and processes of fracturing in rocks is important in characterizing natural and engineered processes related to failure in underground

Y. Lu · L. Wang (✉)
State Key Laboratory for Geomechanics and Deep
Underground Engineering, China University of Mining and
Technology, Xuzhou 221116, Jiangsu,
People's Republic of China
e-mail: cumt_lgwang@163.com

Y. Lu
e-mail: yinlong_lu@163.com

D. Elsworth
EMS Energy Institute, G3 Center and Energy and Mineral
Engineering, Pennsylvania State University,
University Park, PA 16802, USA

engineering, the triggering of volcanic eruptions and in earthquake rupture, among others (Jing 2003).

In terms of their geometry, pre-existing flaws can be classified as either two-dimensional (i.e. a fully penetrating flaw) or three-dimensional (i.e. an internal flaw fully embedded in the rock mass or a surface flaw with part of the flaw front intersecting the surface of the rock mass) (Yin et al. 2014). Extensive experimental and numerical investigations have been conducted on 2-D fracturing on specimens containing single or multiple penetrating pre-existing flaw(s) (Bobet and Einstein 1998; Fujii and Ishijima 2004; Li et al. 2005; Prudencio and Van Sint Jan 2007; Tang and Kou 1998; Vasarhelyi and Bobet 2000; Wong and Chau 1998; Yang and Jing 2011). Basically, two types of cracks result, i.e. wing (tensile) cracks and secondary (shear) cracks, are regularly observed to initiate from the tips of the pre-existing 2-D flaws. The propagation and coalescence of these cracks is observed to be dependent on the geometries of the flaws, the arrangement of the flaws and the frictional coefficient on the flaw surfaces. These observations provide insight into the mechanisms of 2-D fracture evolution. However, pre-existing flaws are generally 3-D in nature and thus 2-D representations may be inadequate in representing true response (Yang et al. 2008). This is the central pretext of this study—to examine pseudo-3D response as a proxy for full-3D response.

Mechanisms of 3-D crack development in rocks are more complex than that in 2-D (Germanovich and Dyskin 2000). Some experimental and numerical investigations have probed the initiation, growth and coalescence of cracks in 3-D. For instance, Dyskin et al. (1994, 2003) performed a series of uniaxial compression tests on transparent resin, cement, PMMA and bore-silicate glass specimens with single pre-existing internal 3-D flaws. In these samples, wing cracks sprouted from the pre-existing flaw and then wrapped around it. Although no secondary cracks resulted, small petal cracks appeared along the pre-existing flaw surface. Similar patterns of wing and petal cracks were also observed by Cannon et al. (1990) and Wong et al. (2004a) in PMMA specimens with a pre-existing half-penny shape surface flaw under uniaxial compression. In addition, biaxial compression tests on transparent resin material containing a single embedded disk-like crack demonstrated the importance of the intermediate principal compressive stress in preventing the wrapping behavior of wing cracks—thereby enabling an

extensive growth of branched cracks that ultimately drive the splitting failure of the specimens (Sahouryeh et al. 2002). Recently, Liang et al. (2012) performed a set of numerical simulations on specimens containing a pre-existing surface flaw under uniaxial compression by a 3-D FEM-based statistical modeling approach (RFPA^{3D}) to investigate the influence of rock heterogeneity and pre-existing flaw orientation on 3D crack initiation and propagation. However, most of the above investigations focus on experiments in idealized model materials that are homogeneous, easy to fabricate and allow optical observation of the propagation process, and they may not reflect the realistic fracturing characteristics and mechanisms in heterogeneous natural rocks.

Up to now, few experiments probe 3-D crack growth in authentic rock. Wong et al. (2004b, 2006) performed a set of experimental studies on crack propagation from pre-existing 3-D surface flaws in rock specimens of marble, sandstone and gabbro under uniaxial compression. In their experiments, a CCD camera was utilized to record the cracking process on the surface of the rock specimens and an acoustic emission system was employed to monitor the crack growth within the specimens. It was reported that a new type of crack initiated and propagated in the opposite direction of conventional wing cracks in real rock specimens and thereby was defined as anti-wing crack. The propagation of anti-wing cracks was found to be closely dependent on the pre-existing flaw geometries and the specimen type. Liu et al. (2008) conducted biaxial compression tests on Fangshan granodiorite specimens with a pre-existing surface flaw and investigated the 3-D propagation process of cracks inside of the specimens by multichannel acoustic emission. More recently, Yin et al. (2014) investigated the coalescence between two parallel 3-D pre-existing surface flaws in granite specimens under uniaxial compression using digital imagery and a digital speckle correlation method (DSCM)—followed by post-mortem sectioning to identify and classify the patterns and nature of crack propagation and coalescence as a function of bridge angle. These experimental studies on real rock materials identify some basic characteristics of 3-D crack growth under compression. Lacking, however, is a systematic study of the impact of flaw geometry on response, together with the codifying of behavior. A major difficulty in realizing this goal is in how to trace crack growth within the optically opaque rock specimen. Some indirect testing techniques, such

as AE monitoring and post-mortem sectioning, have been utilized in previous investigations but they are incapable of accurately reconstructing the realistic 3-D internal fracture structures within rocks.

This study follows a number of experimental and numerical studies conducted to investigate the deformation, strength and failure behavior of the intact sandstone specimens (Yang et al. 2012) or pre-cracked specimens with single or multiple penetrating 2-D flaws under various loading conditions (Yang and Jing 2011; Yang et al. 2013). This extension is to examine the evolution of fractures in 3-D by observing the development from a surface flaw. A series of uniaxial compression experiments are systematically performed for sandstone specimens containing a single pre-existing 3-D surface flaw for various flaw geometries. The failure process is followed by digital imaging, in real time, and post-mortem by X-ray CT. The emphasis of this study is to systematically investigate the influence of the geometric parameters of a single pre-existing 3-D surface flaw, including flaw orientation, flaw depth and flaw angle, on the deformation and strength behavior and to analyze the real-time surface cracking characteristics and the 3-D internal fracture patterns and ultimate failure modes of the specimens under uniaxial compression.

2 Experimental methodology

2.1 Specimen preparation

The specimens used in the present study are of red sandstone collected from Junan County, Linyi City, Shandong Province of China. This sandstone is a fine- to medium-grained and macroscopically homogeneous material with a grain size of 0.10–0.35 mm. X-ray diffraction (XRD) confirms that feldspar, quartz, smectite, zeolite and hematite are the mineral compositions in the sandstone material. The basic physical and mechanical parameters of this sandstone are summarized in Table 1.

Rectangular prismatic specimens with dimensions of 70 mm × 120 mm × 20 mm (width × height × thickness) were cut from a single large rectangular block and in the same orientation. The specimen ends were ground smooth and parallel in order to minimize the end effects. In each specimen, a single 3-D surface flaw created at center height using a thin circular diamond

Table 1 Physical and mechanical properties of sandstone material used in this study

Properties	Values
Bulk density, ρ (kg/m^3)	2380
Porosity	8.6 %
Grain size (mm)	0.10–0.35
Young's modulus, E (GPa)	13.5
Poisson's ratio, υ	0.26
Uniaxial compressive strength, σ_c (MPa)	69.3
Internal cohesion, c (MPa)	16.2
Internal frictional angle, φ (°)	38.8

blade (20 mm or 30 mm diameter) to cut a slot on the surface with an opening of ∼0.5–0.8 mm. Figure 1 illustrates the geometry of the specimens containing a pre-existing 3-D surface flaw. The geometric parameters adopted for a single 3-D surface flaw include flaw length ($2a$), flaw angle (α, the inclined angle of the surface flaw to the horizontal direction) and flaw depth (d, the surface flaw cutting depth).

To investigate the effect of surface flaw geometry on the strength and failure behavior of the sandstone specimens under compression, three groups of specimens (with four cases in each group, see Table 2) were prepared for the experiments by changing the three geometric parameters of the surface flaw, i.e. flaw length ($2a$), flaw angle (α) and flaw depth (d). The parameters used for the test series vary within the following range: (i) $2a = 20$, 30, 40 and 50 mm, (ii) flaw angle $\alpha = 15°$, 45°, 60° and 75°, and (iii) $d = 4$, 8, 12 and 20 mm (i.e. flaw depth ratio $d/t = 0.2$, 0.4, 0.6 and 1.0), as listed in Table 2. In each case, three or more specimens were prepared with the same flaw geometry. A total of 50 specimens were prepared for the uniaxial compression tests in this study.

2.2 Testing procedure

The uniaxial compression tests on all specimens were performed with a conventional servo-controlled testing system with the maximum capacity of 2000 kN and maximum stroke of 10 mm. The tests were performed on dry specimens at room temperature. The specimens were uniaxially loaded under displacement-controlled conditions at a strain rate of 1.0×10^{-5} s^{-1} until ultimate failure. Petroleum jelly was applied at the platen-

Fig. 1 Schematic diagram of sandstone specimen containing a single pre-existing 3-D surface flaw under uniaxial compression. The oblique section I-I shows the depth of the pre-existing 3-D surface flaw. d, $2a$ and α represent the depth, length and inclined angle of the surface flaw, respectively. w, h and t denote the width, height and thickness of the specimen, respectively
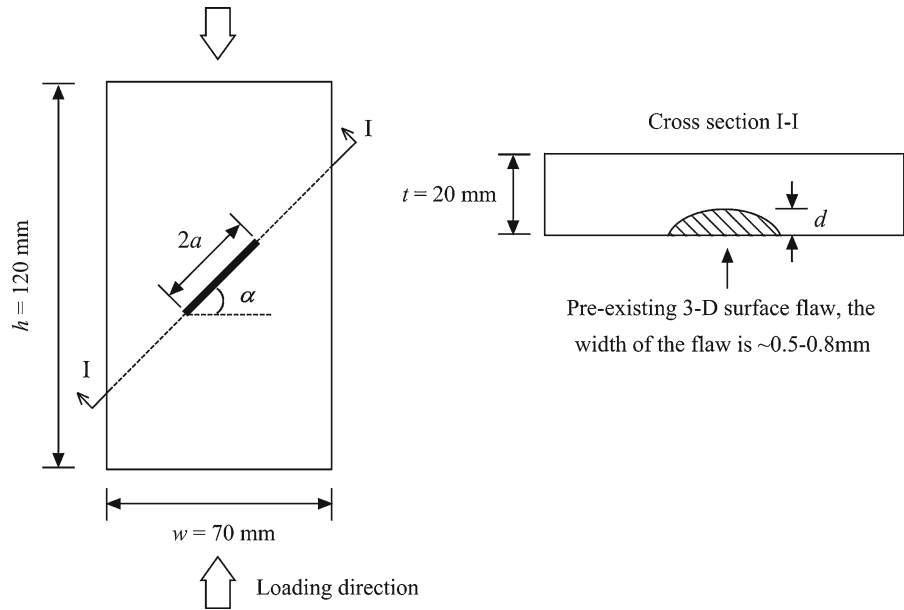
Table 2 Geometric parameters for single pre-existing 3-D surface flaw in sandstone specimens

	Case no.	Flaw length $2a$ (mm)	Flaw angle α (°)	Flaw length d (mm)	Flaw depth ratio d/t	Note
Group 1	1	20	45	8	0.4	Flaw length
	2	30	45	8	0.4	
	3	40	45	8	0.4	
	4	50	45	8	0.4	
Group 2	5	30	15	8	0.4	Flaw angle
	6	30	45	8	0.4	
	7	30	60	8	0.4	
	8	30	75	8	0.4	
Group 3	9	30	45	4	0.2	Flaw depth
	10	30	45	8	0.4	
	11	30	45	12	0.6	
	12	30	45	20	1.0	
Group 4	13	0	N	0	0	Intact specimen

specimen interface to decrease the influence of end friction and platen restraint. Three or more tests were repeated for each case with the same flaw geometry to minimize the dispersion of test results caused by the heterogeneity of specimen material. Load and deformation response of the experiments were recorded simultaneously and in real-time together with high-definition images at a capture rate of 15 frames/s to monitor surface cracking. These images were used to identify the progress of surface cracking. Post-mortem scanning by X-ray CT used a NEWTOM (Italy) CTS machine with

a voxel resolution of 0.25 mm × 0.25 mm × 0.25 mm. The internal 3-D crack patterns together with macroscopic failure modes of the specimens were identified from the CT scanning images.

All of the testing results for the specimens containing a single pre-existing 3-D surface flaw with different geometric parameters under uniaxial compression are presented in the following. Also, the effects of flaw depth, flaw length and flaw angle on the deformation, peak strength, crack growth and ultimate failure modes of the sandstone specimens are discussed in detail.

Fig. 2 Influence of flaw length ($2a =$ 0, 20, 30, 40 and 50 mm) on **a** the axial stress –axial strain response and **b** the uniaxial compressive strength (UCS) for sandstone specimens with the same flaw depth of $d = 8$ mm and flaw angle of $\alpha = 45°$. The denoted *number* in **a** is flaw length. The specimen with a flaw length of $2a = 0$ mm is an intact specimen
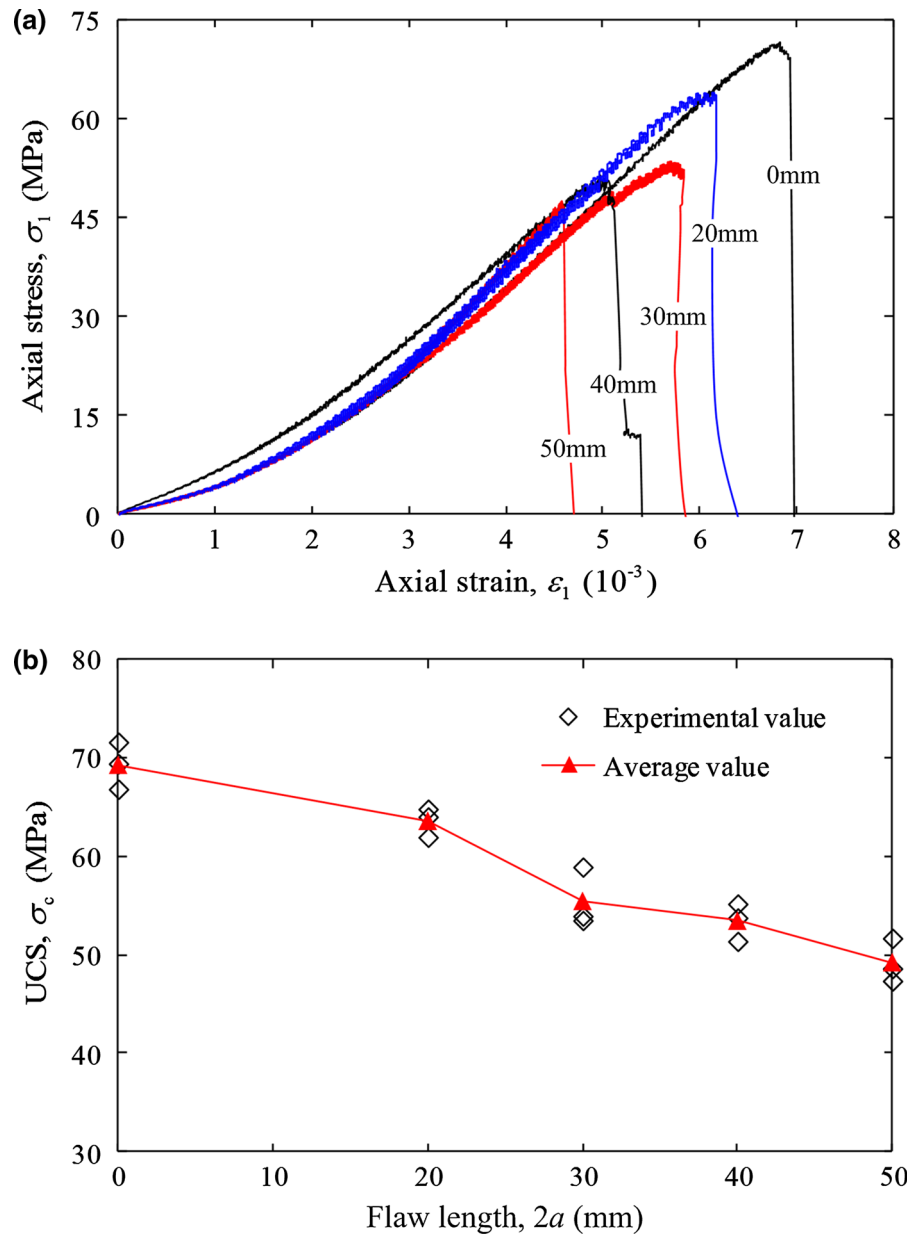
3 Strength and deformation behavior

A typical axial stress–axial strain curve for the specimens with different flaw lengths of $2a = 0$, 20, 30, 40 and 50 mm (the flaw depth is fixed at $d = 8$ mm and the flaw angle is fixed at $\alpha = 45°$) are shown in Fig. 2a, in which the specimen with the flaw length of $2a = 0$ mm is an intact specimen. It is apparent that the axial stress–axial strain behavior of the specimen with a single pre-existing flaw is similar to that of the intact specimen,

which generally exhibits a four-stage behavior. This includes the (i) initial development of cracks and pore closure (the stress–strain curve shows the downward concave), followed by (ii) linear elastic deformation and then non-linear hardening, and (iii) terminating in an abrupt stress drop that eventually progresses to (iv) dynamic brittle rupture. Also, it is apparent that the stress–strain curves of the specimens with various flaw lengths show slight variations in slope before peak strength. This implies that the flaw length has only a

Fig. 3 Influence of flaw angle (α = 15°, 45°, 60° and 75°) on **a** the axial stress–axial strain curves and **b** the UCS for sandstone specimens with the same flaw length of $2a$ = 30 mm and flaw depth of d = 8 mm. The denoted *number* **a** is flaw angle
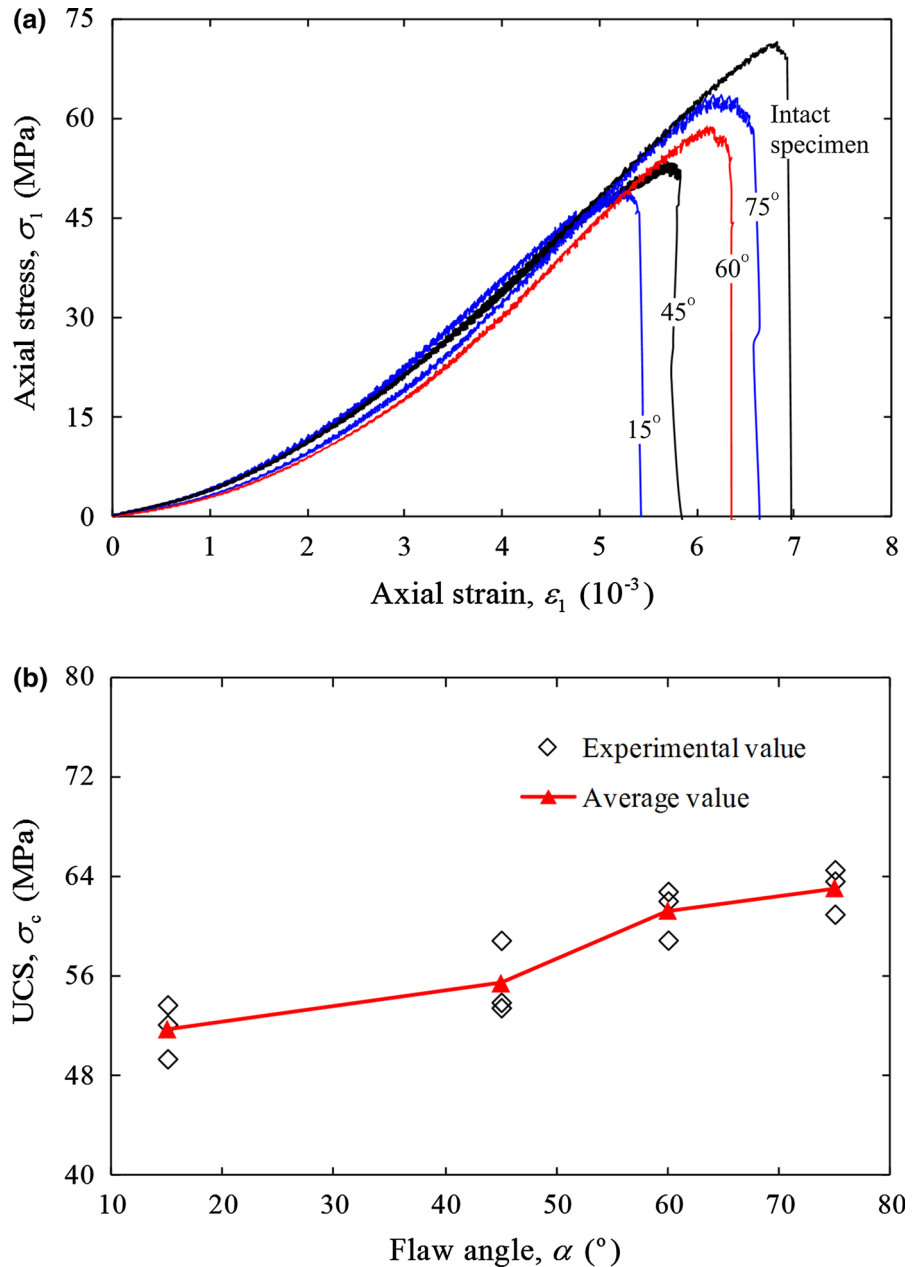
minor effect on the deformation modulus of the specimens. Furthermore, as apparent in Fig. 2a, the uniaxial compressive strength (UCS) of the specimen varies as a function of the flaw length (Fig. 2b)—an increase in the flaw length results in a decrease in the UCS of the specimens. The average UCS of the intact specimen ($2a$ = 0 mm) is 69.28 MPa, while the average UCS of the specimens containing flaws ranges from 63.59 MPa (for $2a$ = 20 mm) to 47.24 MPa (for $2a$ = 50 mm)—a

reduction of 8.2–31.8 % compared to the intact specimen.

Figure 3 depicts the influence of flaw angle (α = 15°, 45°, 60° and 75°) on the axial stress–axial strain curves and the UCS of the specimens with the same flaw length of $2a$ = 30 mm and flaw depth of d = 8 mm. Apparent in Fig. 3 is that the deformation modulus of the specimen is independent of the flaw angle but the UCS of the specimens is significantly controlled by

Fig. 4 Influence of flaw depth ($d =$ 0, 4, 8, 12 and 20 mm) on **a** the axial stress–axial strain curves and **b** the UCS for sandstone specimens with the same flaw length of $2a = 30$ mm and flaw angle of $\alpha = 45°$. The denoted *number* in **a** is flaw depth. The specimen with flaw depth of $d = 0$ mm is an intact specimen
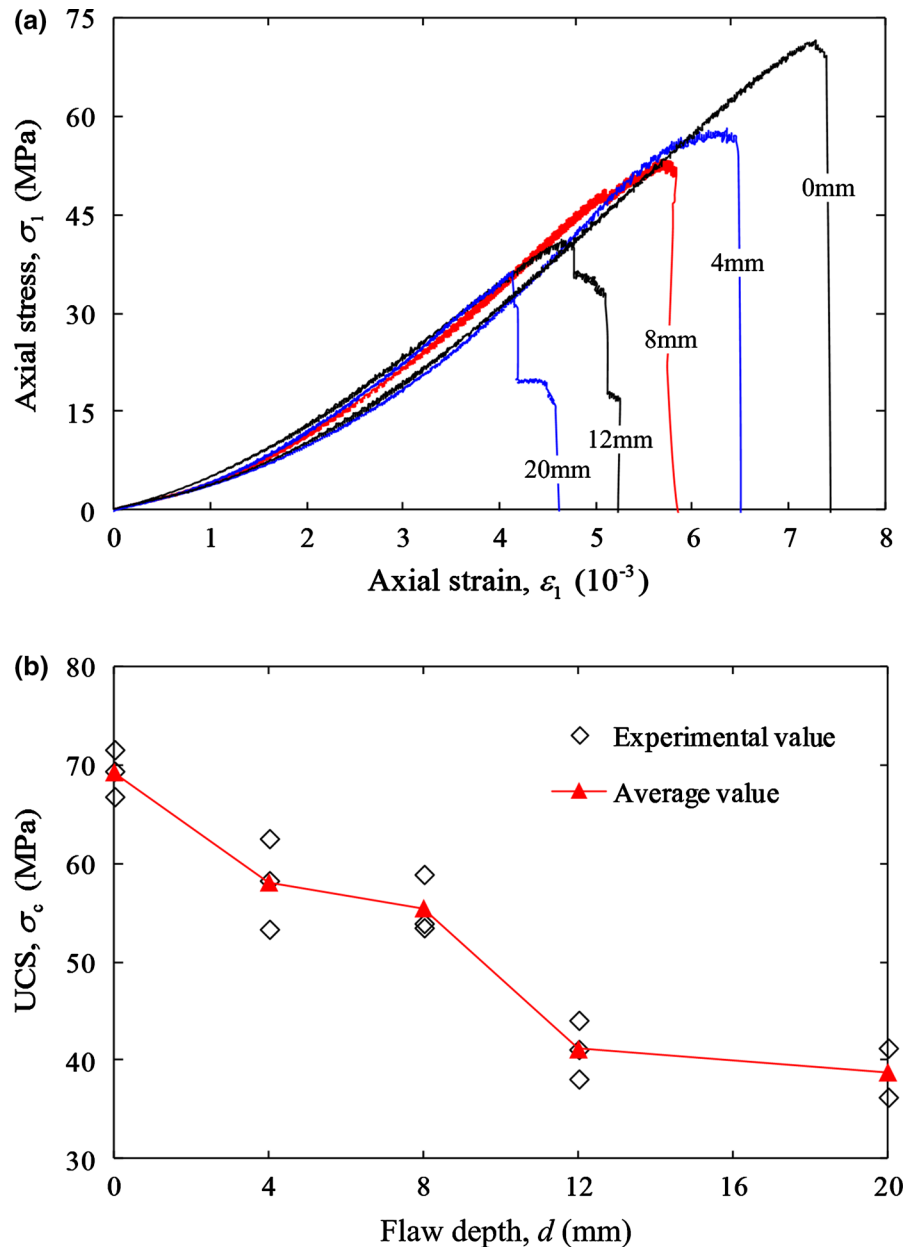
flaw angle. The peak strength of the specimen increases with the increase in the flaw angle (i.e. the dip angle of the flaw to the loading direction decreasing). As the flaw angle increases from $\alpha = 15°$ to $\alpha = 75°$, the averaged UCS of the specimens increases from 49.90 to 63.67 MPa. In addition, the flaw angle is observed to have no effect on the post-peak behavior in the stress–strain curve of the specimens in which the axial stress drops rapidly to zero after peak stress.

The effect of flaw depth ($d = 0, 4, 8, 12$ and 20 mm) on the axial stress–axial strain curves and the UCS of the specimens (the flaw length is fixed at $2a = 30$ mm and the flaw angle is fixed at $\alpha = 45°$) are shown in Fig. 4. Flaw depth has a little influence on the stress–strain behavior before peak strength, but the UCS of the specimens are observed to decrease rapidly from 58.08 MPa to 38.80 MPa with an increase in the flaw depth from $d = 4$ to $d = 20$ mm. More-

Fig. 5 Typical surface cracking patterns from a single pre-existing surface flaw in sandstone specimens: **a** wing cracks, **b** anti-wing cracks and **c** far-field cracks

4 Surface cracking characteristics

In this section, the captured surface images of all tested sandstone specimens in the whole process of deformation were reviewed. The typical surface cracking patterns and the effect of flaw geometry on the surface cracking process were analyzed in detail.
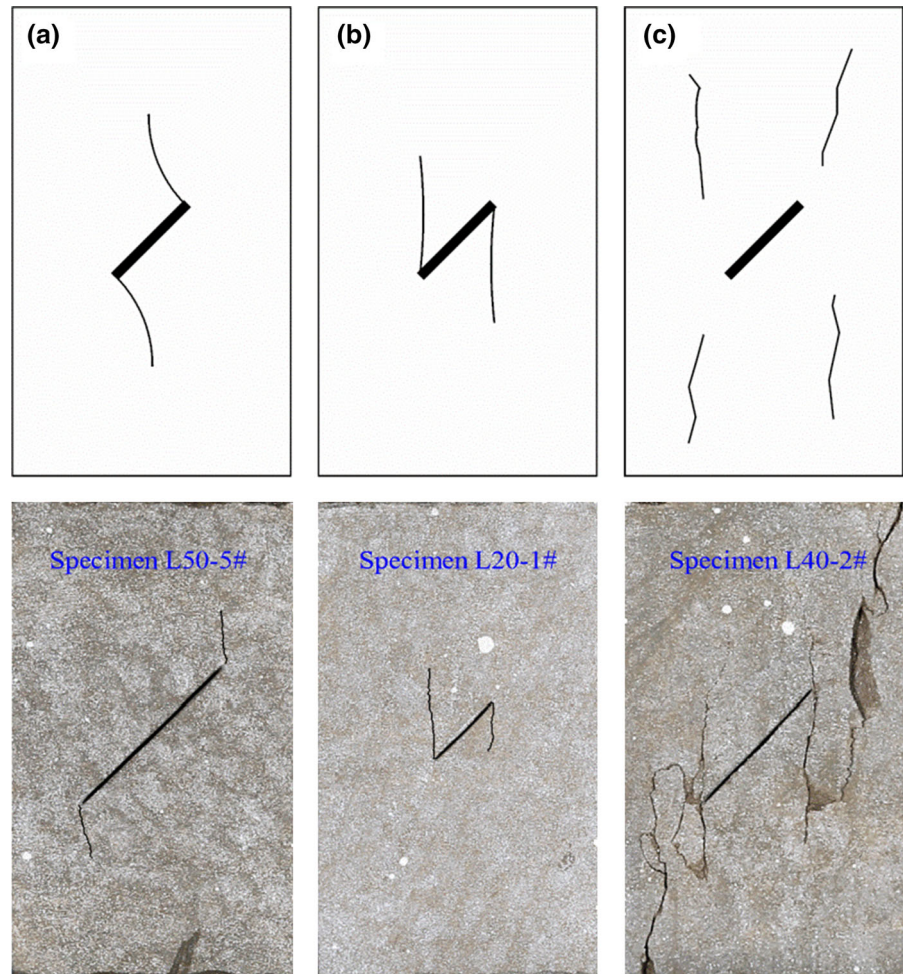
over, it is interesting to note that the post-peak behavior in the stress–strain curve of the specimen is distinctly dependent on the flaw depth. Somewhat surprisingly, the axial stress of the specimen with a shallow flaw depth ($d \leq 8$ mm) drops abruptly to zero after peak stress, whereas the post-peak axial stress of the specimen with a deep flaw ($d > 8$ mm) exhibits distinct steps.

4.1 Classification of surface cracking

The surface images record the evolution of two types of primary cracks—commonly referred to as wing cracks and anti-wing cracks (Wong et al. 2006). These are identified based on their geometries and propagation mechanisms, as shown in Fig. 9a, b. Wing cracks normally initiate from the tips of the pre-existing surface flaws and propagate along a curvilinear path towards the loading direction (see Fig. 5a). Unlike wing cracks, anti-wing cracks generally propagate in the opposite direction to the wing cracks (see Fig. 5b). In addition, another type of crack is observed which usually initiates near the edges of the specimens and is shown in Fig. 5c. We define this type of crack as a far-field crack. The far-field cracks normally appear as secondary cracks after the primary cracks (i.e. wing crack and anti-wing
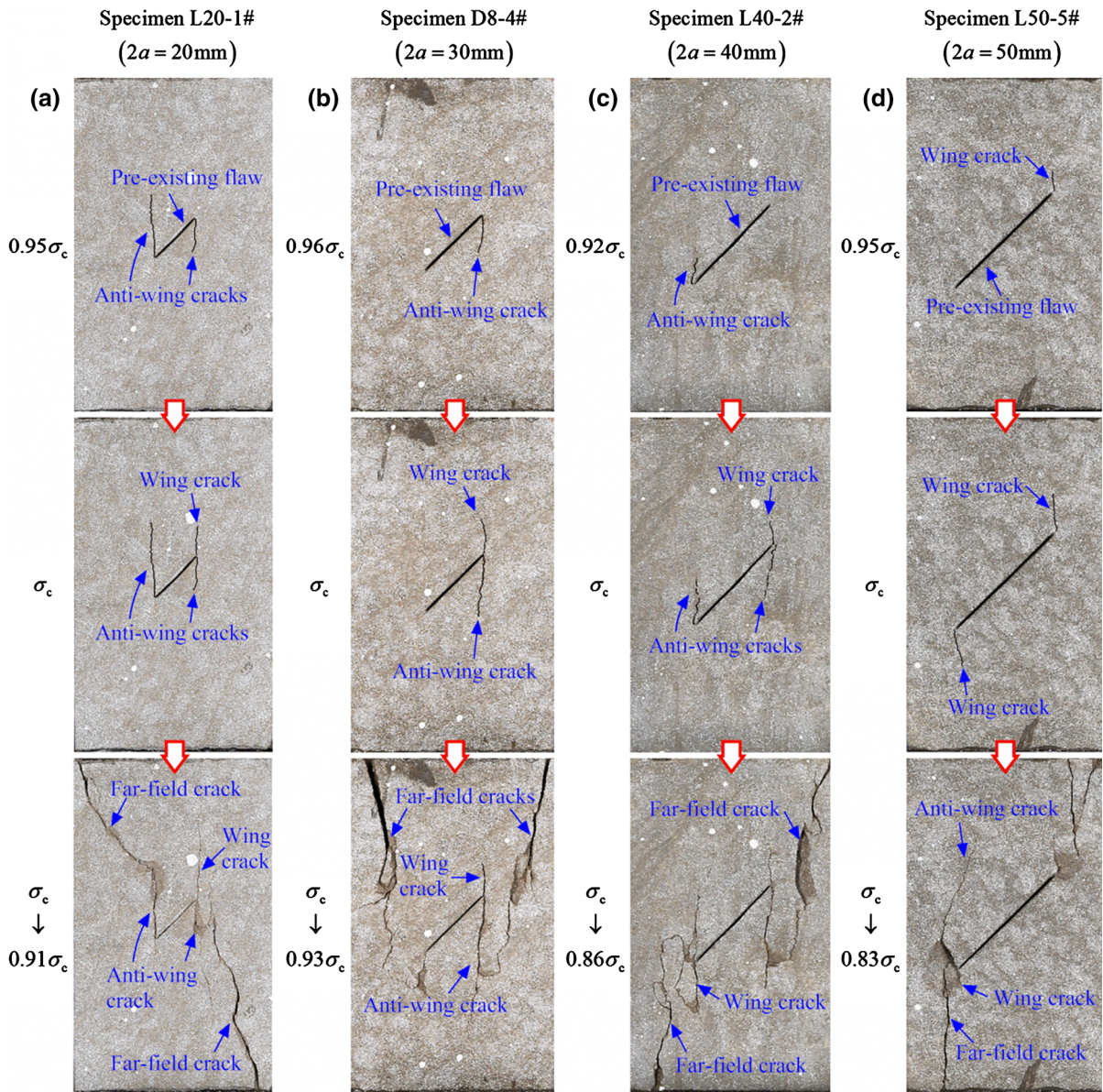
Fig. 6 Crack propagation patterns on the surface of sandstone specimens with various flaw lengths of **a** $2a = 20$ mm, **b** $2a = 30$ mm, **c** $2a = 40$ mm and **d** $2a = 50$ mm (the flaw depth is fixed at $d = 8$ mm and the flaw angle is fixed at $\alpha = 45°$) at different loading levels. σ_c denotes the UCS of the specimen

crack) have developed and they tend to coalesce with the primary cracks to form the ultimate failure of the specimens.

4.2 Effect of flaw length

In accordance with the above crack types, we can further analyze the surface cracking process of the speci-

mens containing a pre-existing surface flaw under uniaxial compression. Figure 6 depicts the typical surface cracking patterns in the specimens with various flaw lengths of $2a = 20, 30, 40$ and 50 mm (the flaw depth is fixed at $d = 8$ mm and the flaw angle is fixed at $\alpha = 45°$) in response to different applied loads. It can be seen that when the flaw length is less than 50 mm (see Fig. 6a–c), the anti-wing cracks appear first in the specimens. As the uniaxial load is increased, the wing

cracks subsequently initiate before the failure of these specimens. In comparison to this, the wing cracks are observed first on the surface of the specimen with a longer flaw length of $2a = 50$ mm and the anti-wing cracks are then only observed to occur after the specimen failure, as shown in Fig. 6d. Such a phenomenon implies that the wing crack is usually easier to initiate from the tip of a longer pre-existing flaw, whereas the anti-wing crack develops readily from the tip of the shorter pre-existing flaw. In addition, it can be further seen from Fig. 6 that both the anti-wing cracks and the wing cracks in all of the specimens appear to arrest at a certain distance from the top or the bottom boundary of the specimens until they become connected to the far-field cracks to form the ultimate failure geometry of the specimen.

4.3 Effect of flaw angle

Figure 7 illustrates the typical crack propagation patterns on the surface of the specimens with different flaw angles of $\alpha = 15°$, $45°$, $60°$ and $75°$ (the flaw length is fixed at $2a = 30$ mm and the flaw depth is fixed at $d = 8$ mm). Apparent from this is that the anti-wing crack is the first crack to initiate in all of the specimens with a flaw angle that varies from $15°$ to $75°$. Also, the stress required for crack initiation increases with an increase in the flaw angle (the angle between the flaw and the loading direction decreasing). As loading is further increased, the wing cracks are observed to initiate later in the specimens with flaw angles of $\alpha = 15°$, $45°$ and $60°$, as shown in Fig. 7a–c. However, no wing cracks are observed in the specimen with a larger flaw angle of $\alpha = 75°$ during the entire process of deformation (see Fig. 7d). This implies that the wing cracks may be difficult to initiate and propagate, as the pre-existing flaw tends to be parallel to the compressive loading direction. Besides, it is clear from Fig. 7 that the propagation length of both the anti-wing cracks and the wing cracks are limited and they eventually coalesce with the far-field cracks—this is responsible for the ultimate failure of the specimen.

4.4 Effect of flaw depth

The effect of flaw depth ($d = 4$, 8, 12 and 20 mm) on the evolution of surface crack propagation patterns in specimens with various flaw depths of $d =$

4, 8, 12 and 20 mm (the flaw length is fixed at $2a = 30$ mm and the flaw angle is fixed at $\alpha = 45°$) are shown in Fig. 8. Anti-wing cracks initiate first in the specimen containing a shallow pre-existing flaw (i.e. $d \leq 8$ mm), as illustrated in Fig. 8a, b, whereas in the specimen with a deep pre-existing flaw (i.e. $d > 8$ mm) the wing cracks turn into the first crack to appear (see Fig. 8c, d). Moreover, the stress required for crack initiation decreases as the flaw depth is increased from $d = 4$ to $d = 20$ mm. This observation implies that a deeper pre-existing flaw enables the easier generation of wing cracks.

Furthermore, it is interesting to note that the fracturing of the specimens that contain an initial penetrating flaw (i.e. $d = 20$ mm) can be regarded as a 2-D problem, in which the anti-wing cracks do not appear during the entire cycle of loading, rather the wing cracks extend to the top and the bottom boundaries of the specimen to induce the ultimate failure (see Fig. 8d) This is significantly different from the 3-D crack initiation and propagation mechanisms in the specimens with the flaw depths of $d = 4$, 8 and 12 mm (see Fig. 8a–c), where neither the wing cracks nor the anti-wing cracks propagate close to the edges of the specimen and the final failure results from the coalescence of the far-field cracks, the wing cracks and the anti-wing cracks.

5 Ultimate failure modes

In the preceding section, the crack propagation patterns on the surface of the specimens were summarized and discussed in detail. However, since the samples are opaque, it is difficult to examine the internal crack structures and the ultimate failure modes from these geometrically-censored 2-D surface images. Therefore, X-ray CT is used following the conventional uniaxial compression tests to further explore the ultimate failure modes of the specimens in 3-D space.

5.1 Effect of flaw length

Figure 9 depicts the CT scanning images of the typical fractured specimens with various flaw lengths of $2a = 20$, 30, 40 and 50 mm (the flaw depth is fixed at $d = 8$ mm and the flaw angle is fixed at $\alpha = 45°$). Shown, are three sections including two cross-sections II-II and III-III and a single longitudinal section I-I,
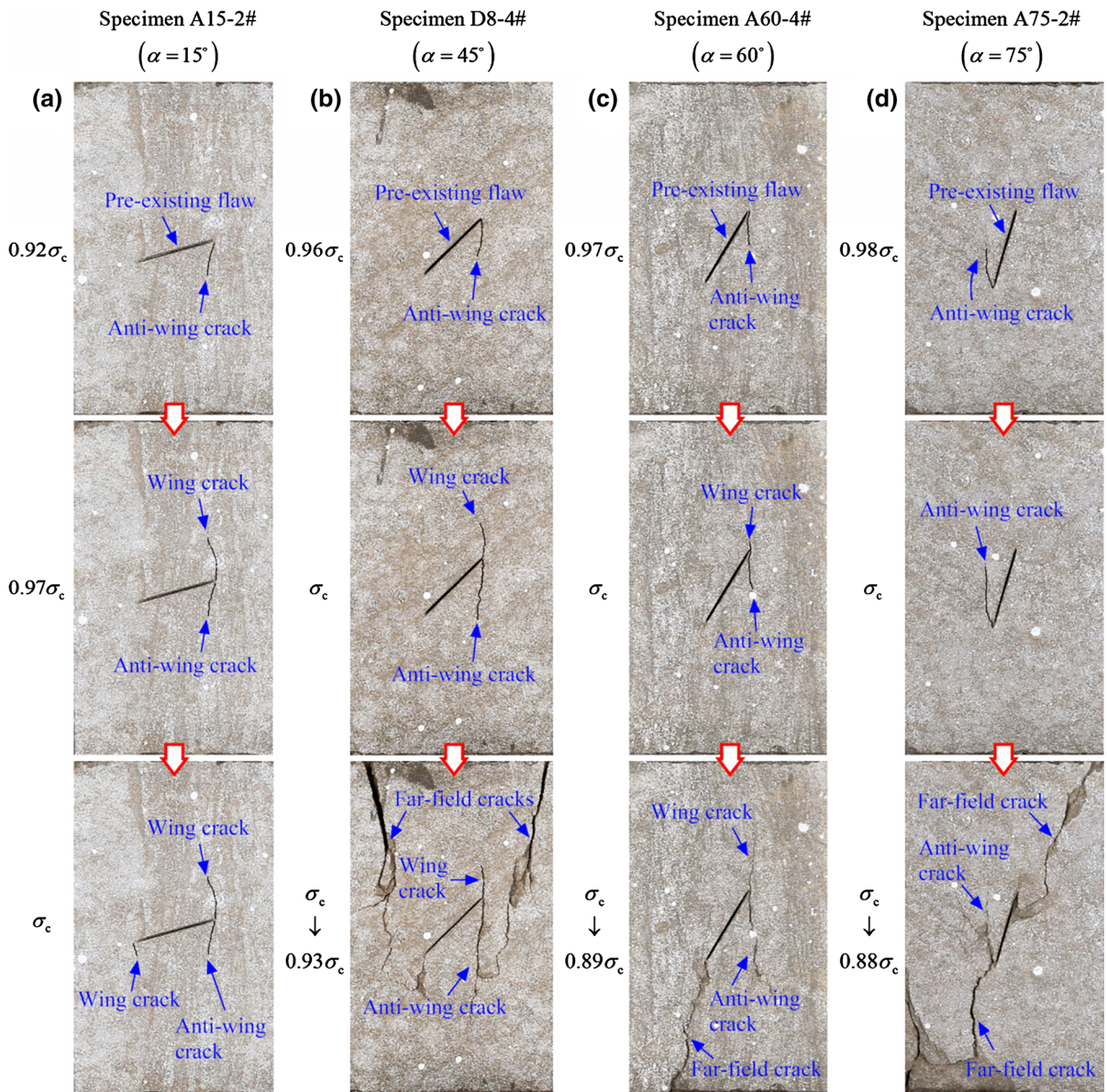
Fig. 7 Crack propagation patterns on the surface of sandstone specimens with various flaw angles of **a** $\alpha = 15°$, **b** $\alpha = 45°$, **c** $\alpha = 60°$ and **d** $\alpha = 75°$ (the flaw depth is fixed at $d = 8$ mm and the flaw length is fixed at $2a = 30$ mm) at different applied stress levels

to illustrate the nature of the 3-D cracks inside of the specimens. From Fig. 9, it is apparent that a typical shell-like crack in 3-D, which is commonly referred to as petal crack, appears within all of the specimens. The petal crack is seen to initiate at the inner (lateral) contour of the pre-existing flaw and propagates along the direction deviated from the maximum compressive stress to ultimately wrap around the flaw (see longitu-

dinal section I-I in Fig. 9). The cross-sectional profile of the petal crack is similar in shape to a semi-ellipse, as shown in cross-section II-II of Fig. 9. Moreover, the boundaries of the petal crack seem to appear on the specimen surface as an anti-wing crack.

In addition to the petal crack, the interior wing crack is also observed within all of the specimens and for all flaw lengths. It is apparent that the wing crack evolves
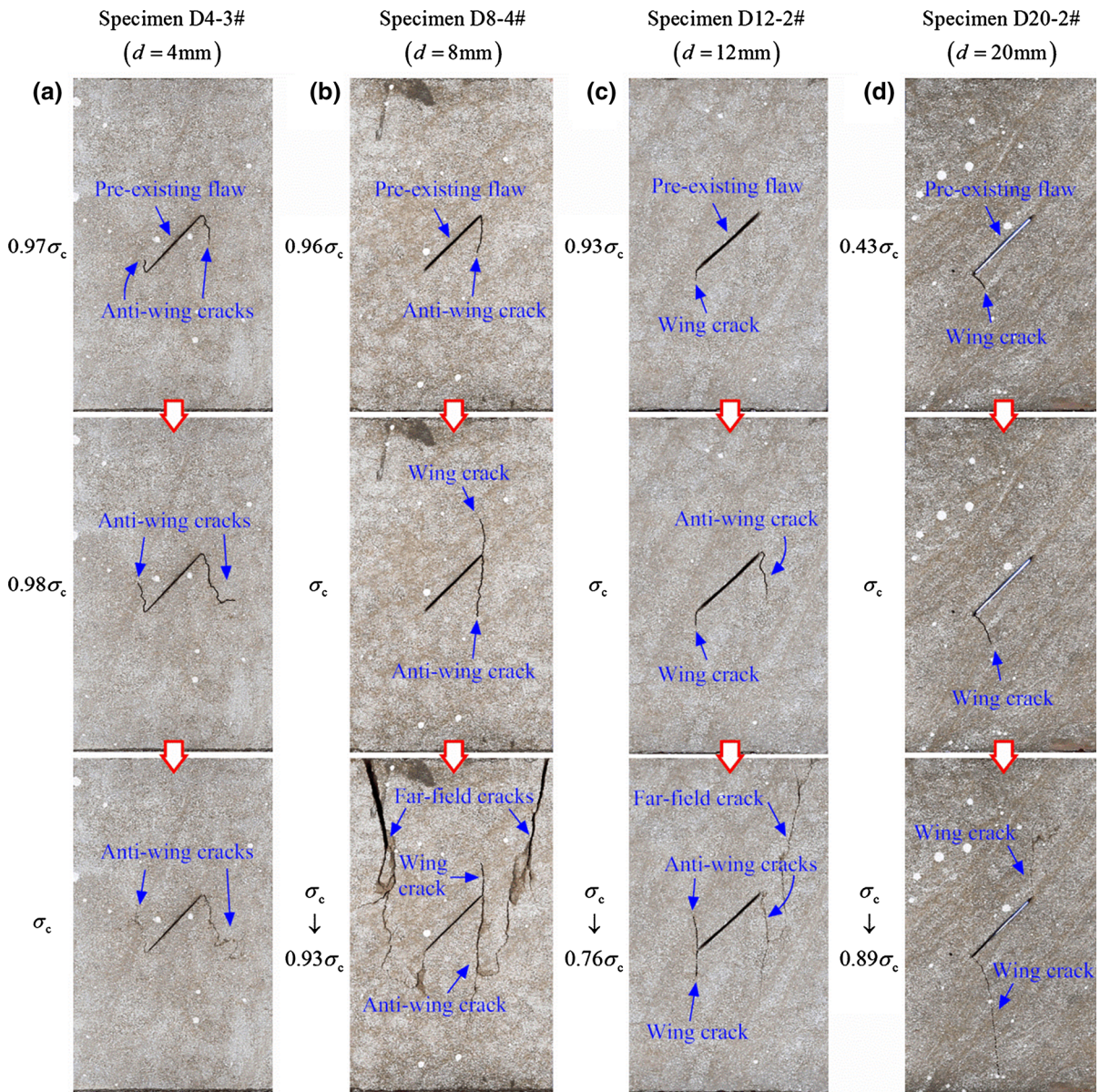
Fig. 8 Crack propagation patterns on the surfaces of sandstone specimens with various flaw depths of **a** $d = 4$ mm, **b** $d = 8$ mm, **c** $d = 12$ mm and **d** $d = 20$ mm (the flaw length is fixed at $2a = 30$ mm and the flaw angle is fixed at $\alpha = 45°$) at different loading levels

from the surface of the specimen into the interior of the specimen and to interact with the petal crack, as shown in cross-section III-III in Fig. 9. In some cases, the wing crack is attached to the petal crack (e.g. see Fig. 9b). This makes it difficult to distinguish the wing crack from the petal. However, it should be pointed out that the appearance of the wing crack is independent of the petal crack. They usually propagate through different parts of the specimen and their growth behaviors are not the same, as shown by, for example, cross-section III-III of Fig. 9d.

The ultimate failure of the specimens is observed to be caused by the coalescence of the petal cracks with the wing cracks together with many small secondary cracks. The secondary cracks are observed to initiate randomly within the intact part of the specimen in either
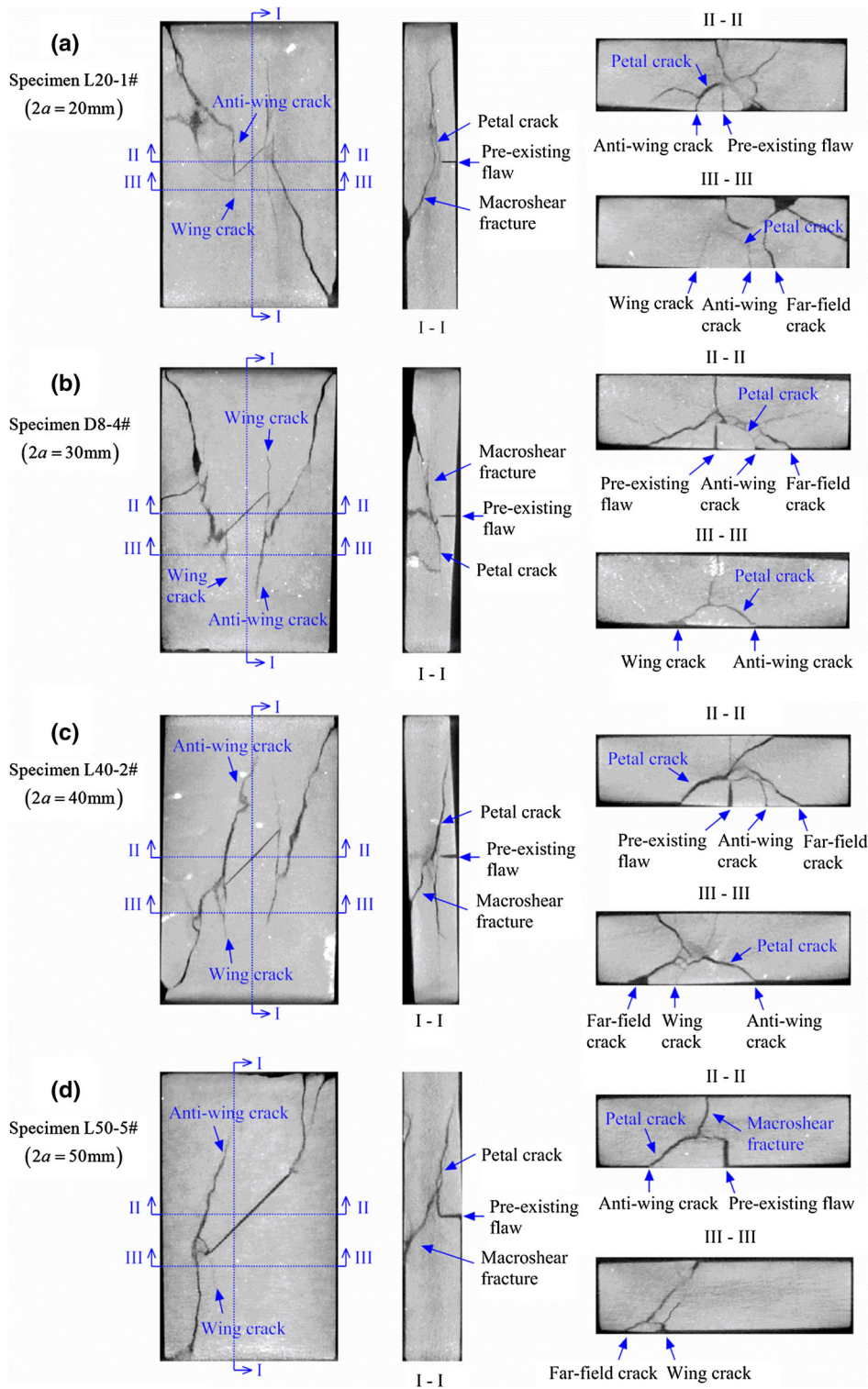
Fig. 9 CT scanning images of the ultimate failure modes of sandstone specimens with various flaw lengths of **a** $2a = 20$ mm, **b** $2a = 30$ mm, **c** $2a = 40$ mm and **d** $2a = 50$ mm (the flaw depth is fixed at $d = 8$ mm and the flaw angle is fixed at $\alpha = 45°$). The sections of *I-I, II-II and III-II* show the crack patterns inside of the fractured specimens

tensile or shear mode and to run to the boundaries of the specimens, as shown in cross-sections II-II and III-III in Fig. 9. Some of the secondary cracks appear on the surface of the specimen as the far-field cracks (e.g. see Fig. 9c). Furthermore, apparent in the longitudinal section I-I in Fig. 9, that regardless of flaw length, the specimens normally exhibit a similar ultimate shear failure mode. Several macro-shear fractures, occurring within the intact part of the specimen, are observed to connect with the petal crack and to eventually divide the specimen into several parts. In addition, it can be further seen from Fig. 9 that the longer flaw length contributes to the petal crack growth—both the long-axis length and the cross-sectional area of the petal crack (on the cross-section of II-II) increase with the flaw length. This may explain why the UCS of the specimen declines with an increase in flaw length.

5.2 Effect of flaw angle

The effect of flaw angle ($\alpha = 15°$, $45°$, $60°$ and $75°$) on the internal crack patterns and the final failure modes of the specimens with the same flaw length of $2a = 30$ mm and flaw depth of $d = 8$ mm is depicted in Fig. 10. Generally, it can be seen from the longitudinal section I-I in Fig. 10 that regardless of flaw angle, all of the specimens rupture essentially in the same shear mode—this is typically a coalescence between the macro-shear fracture and the petal crack.

Furthermore, it is apparent from Fig. 10 that the propagation patterns of the internal cracks are affected by the flaw angle. For the specimen with a steeper flaw angle of $\alpha = 75°$ (the flaw is approximately parallel to the loading direction, see Fig. 10d), no wing cracks are observed inside the ruptured specimen. Also, the petal crack appears to have a restricted propagation and its cross-sectional area is quite small, as shown in cross-section II-II in Fig. 10d. As the flaw angle is decreased (i.e. the angle between the flaw and the loading direction is increased, see Fig. 10a-c), both the wing crack and the petal crack are observed to appear in the specimens. The cross-sectional area of the petal crack (on the cross-section of II-II) expands with a decrease in the flaw angle. In other words, a smaller flaw angle is conducive to the propagation of the petal crack and the wing crack. This likely explains why the UCS of the specimen gradually decreases with a decrease in the flaw angle.

5.3 Effect of flaw depth

Figure 11 illustrates the influence of flaw depth ($d = 4$, 8, 12 and 20 mm) on the evolution of the internal crack patterns and the final failure modes of the specimens (the flaw length is fixed at $2a = 30$ mm and the flaw angle is fixed at $\alpha = 45°$). It is seen that the ultimate failure mode of the specimen with a non-penetrating 3-D flaw (i.e. $d < 20$ mm) is significantly different from that with a penetrating 2-D flaw (i.e. $d = 20$ mm). In the 3-D state, the specimen usually exhibits a shear failure mode which is closely related to the propagation and coalescence of the internal cracks (see Fig. 11a–c), whereas, in the 2-D state, the specimen normally ruptures in a tensile splitting mode which results from the induced wing cracks penetrating approximately vertically into the specimen without curling inside and extending to the top and the bottom boundaries of the specimen, as shown in Fig. 11d.

Besides, apparent from the longitudinal section I-I and the cross-section II-II in Fig. 11a–c the petal crack appears to propagate a longer distance within the specimen and its cross-sectional area (on the cross-section of II-II) is expands with an increased depth of the initial flaw. This observation may explain why the UCS of the specimens decreases with increasing flaw depth. Also, the ultimate failure mode of the specimen shows an increasing dependency on the growth of petal cracks with an increase in initial flaw depth. When the flaw depth is shallower ($d = 4$ mm), the specimen exhibits a shear failure mode similar to the intact specimen (see Fig. 11a). The petal crack seems to have no influence on the macro-shear fracture, due to its very limited growth and restricted length. While for the specimen with a flaw depth of $d = 8$ mm (see Fig. 11b), the interaction between the macro-shear fracture and the petal crack are mainly responsible for the ultimate failure of the specimen. Moreover, as the flaw depth is further increased to $d = 12$ mm (see Fig. 11c), the petal cracks tends to dominate the macroscopic failure of the specimen. Such effects of the flaw depth on the ultimate failure mode essentially result from the contribution of the flaw depth to the propagation of the petal crack.

6 Fracture mechanisms of the 3-D surface flaw

From the above experimental results, several new types of cracks, including petal cracks, wing cracks and anti-
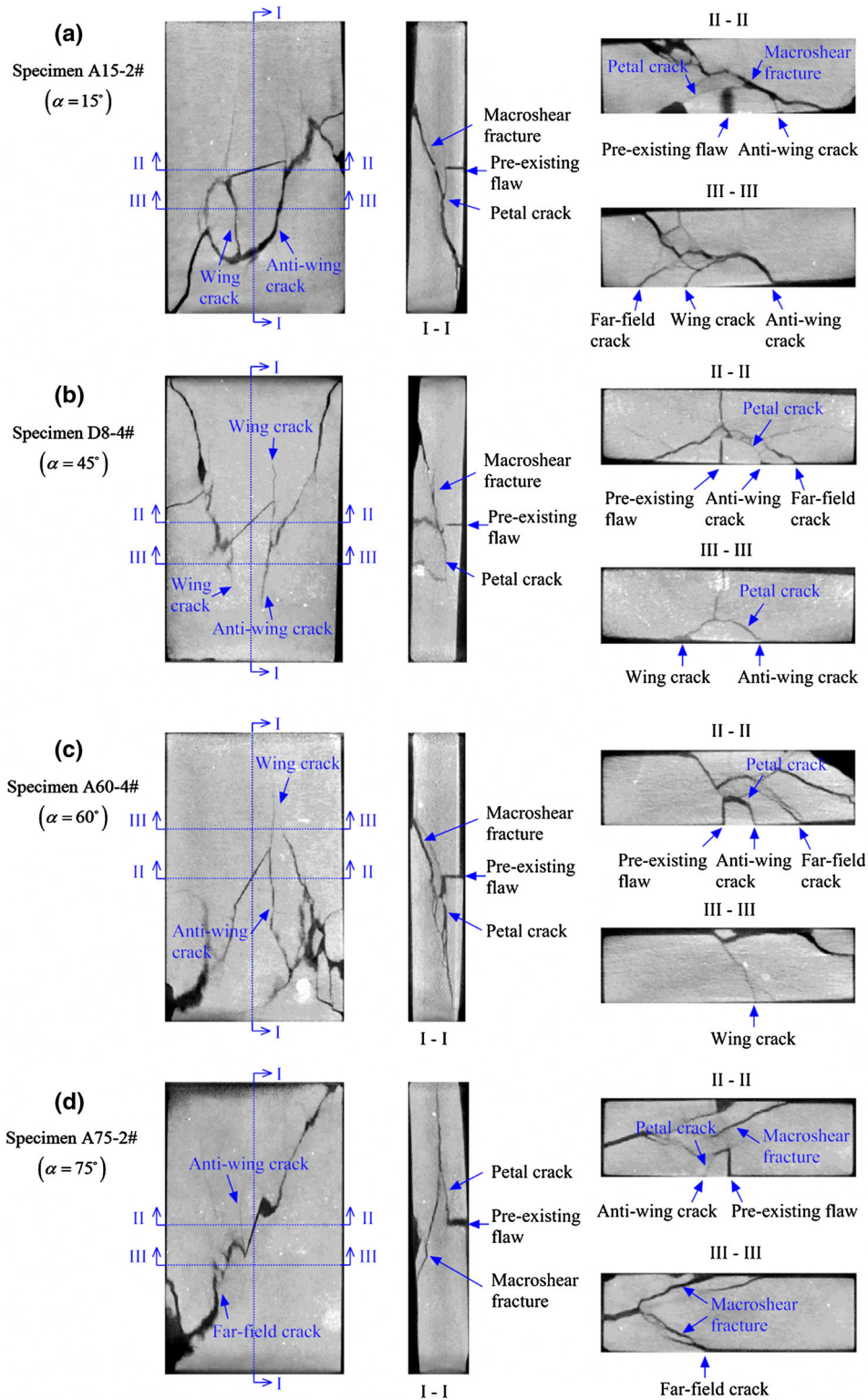
Fig. 10 CT scanning images of the ultimate failure modes of sandstone specimens with various flaw angles **a** $\alpha = 15°$, **b** $\alpha = 45°$, **c** $\alpha = 60°$ and **d** $\alpha = 75°$ (the flaw length is fixed at $2a = 30$ mm and the flaw depth is fixed at $d = 8$ mm)
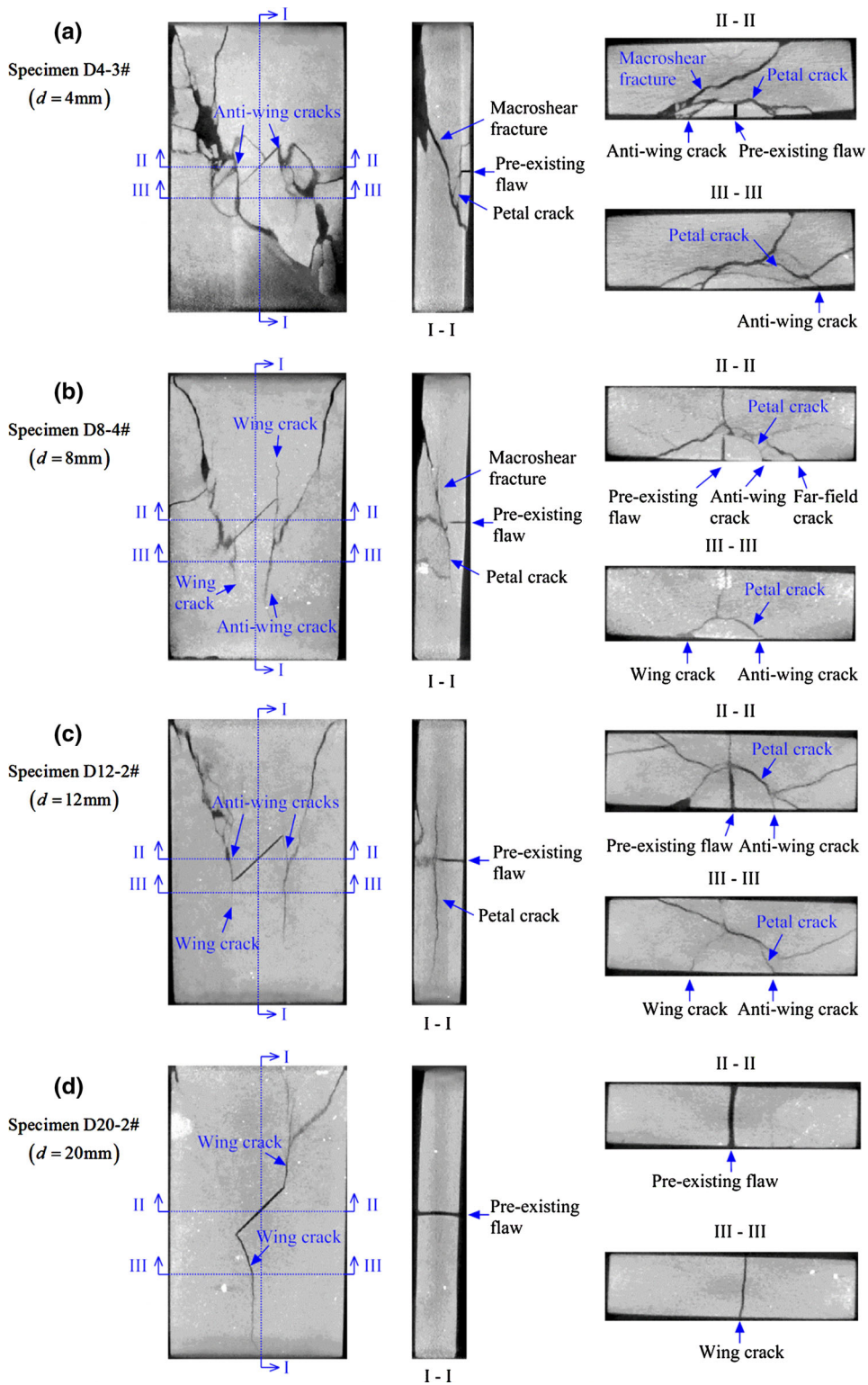
Fig. 11 CT scanning images of the ultimate failure modes of sandstone specimens with various flaw depths of **a** $d = 4$ mm, **b** $d = 8$ mm, **c** $d = 12$ mm and **d** $d = 20$ mm (the flaw length is fixed at $2a = 30$ mm and the flaw angle is fixed at $\alpha = 45°$)

Fig. 12 Stress state around a pre-existing 3-D surface flaw subjected to far-field uniaxial compression
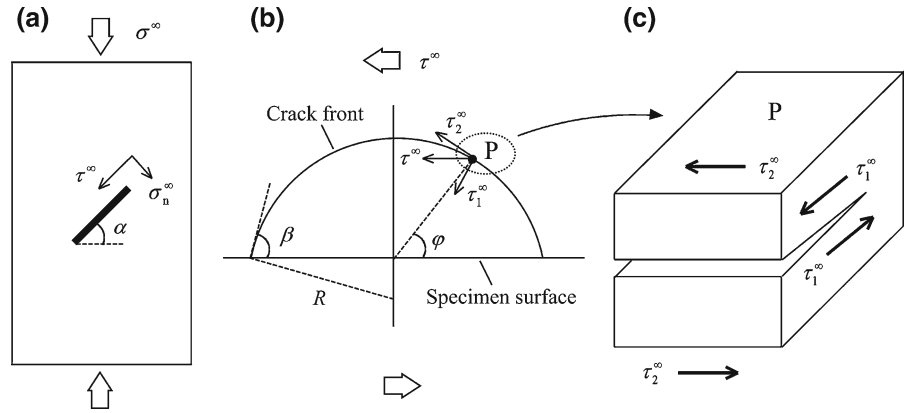
wing cracks, are observed to initiate from the pre-existing 3-D surface flaw in the specimens of sandstone under uniaxial compression. These fracture patterns and mechanisms of the 3-D surface flaw are more complex than those of 2-D penetrating flaw. In the following, we briefly analyze and discuss the fracture behavior of the 3-D surface flaw based on the classical fracture mechanics theory.

For the pre-cracked specimens under uniaxial compression in our experiments (see Fig. 12a), the far-field compressive stress (σ^∞) can be decomposed into a shear stress component (τ^∞) parallel to the pre-existing flaw face and a normal compressive stress component (σ_n^∞) perpendicular to the flaw face. Since the pre-existing surface flaw is created by cutting a slot on the specimen surface with a diamond saw blade, the flaw has a large opening of ~0.5–0.8 mm. The normal compressive stress component (σ_n^∞) is not large enough to close such pre-existing flaw, so that there is no frictional contact between the flaw faces. Thus, the shear stress component (τ^∞) appears to contribute largely to the pre-existing flaw initiation and propagation.

The shear stress component (τ^∞) can be further divided into normal and tangential components (τ_1^∞ and τ_2^∞) along the pre-existing flaw front, as shown in Fig. 12b. It is obvious that the two shear components cause different cracking mechanisms (see Fig. 12c). At point P, τ_1^∞ performs mode II shear loading (i.e. sliding mode), whereas τ_2^∞ induces mode III anti-plane shear loading (i.e. tearing mode). To further analyze the fracture behavior caused by the shear loading (mode II–III), it needs to calculate the stress intensity factor (SIF) of the surface flaw. However, until now, the analytical solution for the SIF around a 3-D partially circular surface crack under far-field shear stress has remained

unknown. By fitting the data extracted from the finite element analysis by Murakami and Natsume (2002), Chau et al. (2004) obtained an approximate solution for the SIF around a partially circular surface crack with $\beta = 67°$ and $v = 0.3$ (β is the intersection angle between the crack front and the specimen surface and v is the Poisson's ratio), which is:

$$\begin{cases} K_{\rm II} = \tau^\infty \sqrt{\pi R}\big(-0.083\varphi^4 + 0.46\varphi^3 \\ \qquad\quad - 0.89\varphi^2 + 0.33\varphi + 0.41\big) \\ K_{\rm III} = \tau^\infty \sqrt{\pi R}\big(0.42\varphi^4 - 1.30\varphi^3 \\ \qquad\quad + 1.17\varphi^2 - 0.12\varphi + 0.28\big) \end{cases} \quad (1)$$

where $K_{\rm II}$ and $K_{\rm III}$ are mode II and mode III stress intensity factors, R is the radius of the surface crack and φ is the angle in radians (see Fig. 12b).

Figure 13 shows the variation of the stress intensity factors ($K_{\rm II}$ and $K_{\rm III}$) along the surface crack front ($\beta = 67°$ and $v = 0.3$). From Fig. 13, it is seen that $K_{\rm II}$ equals zero at the deepest point of the crack front ($\varphi = 90°$) and it gradually increases while approaching the specimen surface (i.e. φ decreasing). The maximum of $K_{\rm II}$ occurs at φ of about 5°–15°. But on the other hand, $K_{\rm III}$ reaches its maximum value at the deepest point of the crack front ($\varphi = 90°$) and it gradually decreases while approaching the specimen surface. These results imply that the effect of mode II shear sliding dominates near the two tips of the surface flaw (close to the specimen surface), whereas the effect of mode III anti-plane tearing dominates along the deep front of the surface crack. According to our experimental observation, the petal cracks initiate along the inner contour of the pre-existing flaw, while the wing cracks nucleate from the upper and lower tips of the flaw. Thus, it could be conclude that the observed petal
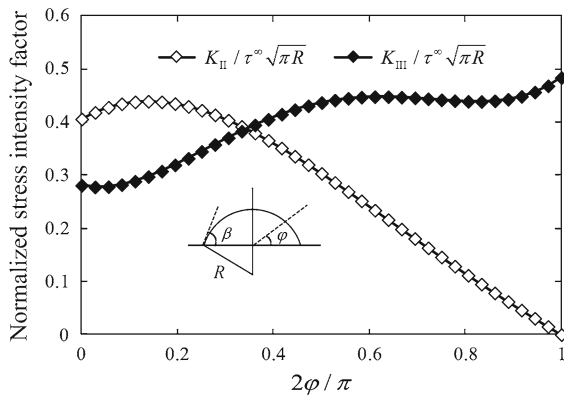
Fig. 13 Normalized stress intensity factors (K_{II} and K_{III}) along a 3-D partially circular surface crack front under far-field shear stress. The intersection angle between the crack front and the free surface is $\beta = 67°$ and the Poisson's ratio is $v = 0.3$

cracks are mainly caused by the mode III tearing effect, whereas the wing cracks are mainly attributed to the mode II shear sliding effect. Based on this understanding, if the pre-existing flaw penetrates the specimen completely (i.e. 2-D flaw), then the mode III tearing effect will disappear. That's why no petal cracks are observed in the specimens containing a penetrating 2-D flaw in our experiments. In contrast, if the pre-existing flaw is a non-penetrating 3-D surface flaw with shallow flaw depth, then the shear sliding of the flaw will be restricted to a large extent by the intact portion along the flaw front embedding inside the specimen, thus making the wing cracks difficult to initiate from the two tips of the pre-existing flaw. This may explain why no wing cracks are observed in the specimens with a shallower flaw depth of $d = 4$ mm in our experiments. However, for the specimens with a deeper 3-D surface flaw, the wing cracks are likely to nucleate after the initiation of the petal cracks. This is because the propagation of the petal crack will release, to a certain extent, the restriction of the shear sliding along the pre-existing flaw face.

It is worth noting that although the shear loading is mainly responsible for the growth of the petal and wing cracks, neither of the two cracks is a shear fracture mode. Our experiments found that both the petal and wing cracks are results of crack branching phenomenon (i.e. crack propagates along a direction deviating from the pre-existing surface flaw plane). It seems that the shear loading does not result in a mode II or mode III shear fracturing. The two observed cracks most likely result from the local tensile stress at the flaw tip induced

by the shear loading (Liang et al. 2012). Such phenomenon may be explained by the fact that rocks are typically brittle materials, having much higher shear strength than tensile strength. Thus, tensile fracture may more likely occur under the shear loading (Rao et al. 2003).

In addition to the effect of the far-field shear stress component (τ^{∞}), the far-field normal compressive stress component (σ_n^{∞}) in our experiments is also likely to affect the initiation and propagation of the petal and wing cracks. In traditional fracture mechanics, a flaw (or a crack) is commonly assumed to have no thickness. However, the influence of the thickness of the pre-existing flaw in our experiments (the flaw opening is ∼0.5–0.8 mm) cannot be ignored. Due to the opening of the pre-existing flaw, the normal compressive stress component (σ_n^{∞}) causes more complex local shear and tensile stress field at the flaw tip (Li and Wong 2012; Liang et al. 2012), as shown in Fig. 14. The resulting local stress field would induce potential shear and tensile fractures parallel to the flaw tip wall, which also contributes to the initiation and propagation of the petal and wing cracks. In general, the petal and wing cracks may be induced by mixed-mode loading.

Apart from the petal and wing cracks inside of the specimens, we also observed another interesting surface cracking pattern, i.e. anti-wing cracks, which propagates in the opposite direction to the typical wing cracks. Our X-ray CT scanning of the specimens reveal that the anti-wing cracks appearing on the specimen surface are connected to the internal petal cracks. Wong et al. (2008) and Liu et al. (2008) also indirectly observed the same phenomenon by AE monitoring tests. Based on this phenomenon, we can conclude that the anti-wing crack is not isolated, and it is most likely to be the trace outlet from the internal petal crack propagation on the specimen surface. When the petal cracks gradually propagate from the inner contour of the pre-existing flaw to the specimen surface (with a tendency to wrap around the pre-existing flaw), a shell-shaped block is developed between the petal cracks and the pre-existing flaw and it tends to erupt from the specimen. This results in a strong mixed tensile-shear effect along the boundaries of the petal cracks. Such mixed tensile-shear effect could be responsible for the initiation and propagation of the anti-wing crack (Wong et al. 2008; Yin et al. 2014).

However, due to the complexity of 3-D stress field in the fractured specimens, it is very challenging to

Fig. 14 Local stress field and potential fracture mode for an opening flaw under normal compression
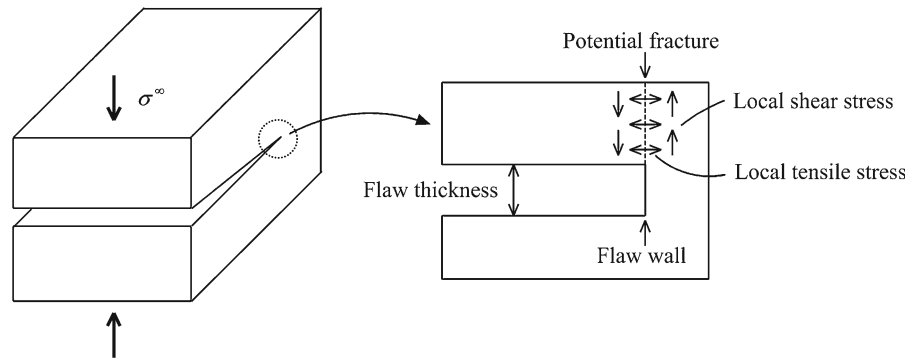
establish a quantitative model to accommodate the surface cracking as well as the internal 3-D fracturing process. More theoretical and numerical work remains to be done to comprehensively investigate the fracturing behavior of the 3-D surface flaw.

7 Conclusions

In this study, a series of uniaxial compression experiments were conducted on specimens of sandstone containing a single pre-existing 3-D surface flaw in various configurations. Failure process was imaged on the surface by photographic monitoring and X-ray computerized tomography (CT) was used to probe the inside, post-mortem. The effects were systematically examined of the geometry of a single flaw including flaw length, flaw angle and flaw depth on the fundamental behaviors of deformation, strength, crack growth and ultimate failure. The following conclusions can be drawn.

The geometry of a pre-existing surface flaw is observed to have minor influence on the stress–strain behavior before peak strength (e.g. deformation modulus), but to exert a significant effect on the UCS of the specimens. UCS drops of 25.7, 33.2 and 21.6 % were observed due to an increase in the flaw length ($2a = 20$–50 mm) and flaw depth ($d = 4$–20 mm) but a decrease in the inclination of the flaw ($\alpha = 75°$–$15°$). Moreover, it is found that the post-peak behavior in the stress–strain curve of the specimens is insensitive to the flaw length and flaw angle but is closely dependent on the flaw depth—the axial stress of the specimens containing a shallow flaw drops abruptly to zero after peak stress but that of the specimens with deep flaw exhibits distinct stress-decrement steps post-failure.

Three typical surface cracking patterns are identified and classified by digital photography. These include the evolution of wing cracks, anti-wing cracks and far-field cracks. It is observed that the appearance of wing cracks and anti-wing cracks have a close relation to the geometry of the pre-existing surface flaw. Wing cracks initiate more easily from longer pre-existing flaws and those of deeper flaw depth or smaller flaw angle—anti-wing cracks develop more easily in the converse situation. Importantly, it is found that the stress required for crack initiation on the specimen surface has no clear relation with the flaw length, but it appears to decrease with an increase in flaw depth or a decrease in the flaw inclination. In addition, in the specimen containing a pre-existing fully-penetrating 2-D flaw the wing cracks are found to reach the top and the bottom boundaries and to induce the ultimate failure of the specimen. However, in the specimens with a pre-existing 3-D surface flaw, neither the wing cracks nor the anti-wing cracks could grow close to the edges of the specimens and the ultimate failure of the specimens result from the coalescence of the far-field cracks, wing cracks and anti-wing cracks.

The internal crack structures and the ultimate failure modes of the specimens are reconstructed in 3-D space by CT scanning. It is found that a typical shell-like 3-D internal crack pattern, i.e. the petal crack, initiates at the inner contour of the pre-existing surface flaw and propagates along the direction of the maximum local compressive stress to wrap around the initial flaw. From this, one of the boundaries of the petal crack is observed to appear on the specimen surface as an anti-wing crack. A longer flaw length, deeper flaw depth or smaller flaw angle are observed to contribute to the propagation of the petal crack. In addition, the wing cracks appearing on the surface of the specimen are found to extend into the interior of the specimen and

to interact with the petal crack. The ultimate failure of the specimens are found to result from the coalescence of the petal cracks, the wing cracks together with many small secondary cracks which initiate randomly within the intact part of the specimens either in tensile mode or in shear mode. Moreover, it is observed that the ultimate failure mode of the specimens generally exhibit a combined shear mode, regardless of the flaw length and the flaw angle, but the ultimate failure mode appears to depend distinctly on the flaw depth. The specimen containing a penetrating 2-D flaw normally ruptures in a tensile splitting mode, but the specimens with a non-penetrating 3-D flaw generally fail in a shear mode which shows an increased dependency on the petal crack with the flaw depth increasing.

It is concluded that the fundamental behavior of real rocks materials containing a pre-existing 3-D surface flaw is much more complex than more homogeneous materials containing a thoroughgoing 2-D flaw. However, this study only presents a limited first phase of fracture behavior of 3-D surface flaw with narrowly selected geometry configurations. What has been described in this study can serve as a basis for further tests and the development of analytical and numerical models.

References

Bobet A, Einstein H (1998) Fracture coalescence in rock-type materials under uniaxial and biaxial compression. Int J Rock Mech Min 35:863–888

Cannon N, Schulson E, Smith TR, Frost H (1990) Wing cracks and brittle compressive fracture. Acta Metall Mater 38:1955–1962

Chau K et al (2004) Three-dimensional surface cracking and faulting in Dangan islands area, South of Hong Kong. In: Proceedings of third international conference on continental earthquakes, Beijing, China, pp 12–14

Dyskin A, Jewell R, Joer H, Sahouryeh E, Ustinov K (1994) Experiments on 3-D crack growth in uniaxial compression. Int J Fract 65:R77–R83

Dyskin AV, Sahouryeh E, Jewell RJ, Joer H, Ustinov KB (2003) Influence of shape and locations of initial 3-D cracks on their growth in uniaxial compression. Eng Fract Mech 70:2115–2136. doi:10.1016/S0013-7944(02)00240-0

Fujii Y, Ishijima Y (2004) Consideration of fracture growth from an inclined slit and inclined initial fracture at the surface of rock and mortar in compression. Int J Rock Mech Min 41:1035–1041. doi:10.1016/j.ijrmms.2004.04.001

Germanovich LN, Dyskin AV (2000) Fracture mechanisms and instability of openings in compression. Int J Rock Mech Min 37:263–284. doi:10.1016/S1365-1609(99)00105-7

Horii H, Nematnasser S (1986) Brittle failure in compression: splitting, faulting and brittle-ductile transition. Philos Trans R Soc Lond 319:337–374. doi:10.1098/rsta.1986.0101

Jing L (2003) A review of techniques, advances and outstanding issues in numerical modelling for rock mechanics and rock engineering. Int J Rock Mech Min 40:283–353. doi:10.1016/s1365-1609(03)00013-3

Li H, Wong LNY (2012) Influence of flaw inclination angle and loading condition on crack initiation and propagation. Int J Solids Struct 49:2482–2499. doi:10.1016/j.ijsolstr.2012.05.012

Li Y, Chen L, Wang Y (2005) Experimental research on precracked marble under compression. Int J Solids Struct 42:2505–2516

Liang ZZ, Xing H, Wang SY, Williams DJ, Tang CA (2012) A three-dimensional numerical investigation of the fracture of rock specimens containing a pre-existing surface flaw. Comput Geotech 45:19–33. doi:10.1016/j.compgeo.2012.04.011

Liu L, Liu P, Wong H, Ma S, Guo Y (2008) Experimental investigation of three-dimensional propagation process from surface fault. Sci China Ser D Earth Sci 51:1426–1435

Murakami Y, Natsume H (2002) Stress singularity at the corner point of 3-D surface crack under mode II loading. JSME Int J Ser A 45:161–169

Peng S, Johnson AM (1972) Crack growth and faulting in cylindrical specimens of Chelmsford granite. Int J Rock Mech Min 9:37–86. doi:10.1016/0148-9062(72)90050-2

Prudencio M, Van Sint Jan M (2007) Strength and failure modes of rock mass models with non-persistent joints. Int J Rock Mech Min 44:890–902. doi:10.1016/j.ijrmms.2007.01.005

Rao Q, Sun Z, Stephansson O, Li C, Stillborg B (2003) Shear fracture (Mode II) of brittle rock. Int J Rock Mech Min 40:355–375

Sahouryeh E, Dyskin AV, Germanovich LN (2002) Crack growth under biaxial compression. Eng Fract Mech 69:2187–2198. doi:10.1016/S0013-7944(02)00015-2

Tang CA, Kou SQ (1998) Crack propagation and coalescence in brittle materials under compression. Eng Fract Mech 61:311–324. doi:10.1016/s0013-7944(98)00067-8

Vasarhelyi B, Bobet A (2000) Modeling of crack initiation, propagation and coalescence in uniaxial compression. Rock Mech Rock Eng 33:119–139

Wong RHC, Chau KT (1998) Crack coalescence in a rock-like material containing two cracks. Int J Rock Mech Min 35:147–164

Wong RHC, Huang ML, Jiao MR, Tang CA, Zhu WS (2004a) The mechanisms of crack propagation from surface 3-D fracture under uniaxial compression. Key Eng Mater 261:219–224

Wong RHC, Law CM, Chau KT, Zhu WS (2004b) Crack propagation from 3-D surface fractures in PMMA and marble specimens under uniaxial compression. Int J Rock Mech Min 41:360. doi:10.1016/j.ijrmms.2003.12.065

Wong RHC, Guo YS, Chau KT, Zhu WS, Li SC (2006) Anti-wing crack study from 3D surface flaw in real rock. In:

Proceedings of the 16th European conference on fracture, Alexandroupolis, Greece, pp 825–826

Wong R, Guo Y, Liu L, Liu P, Ma S (2008) Nucleation and growth of anti-wing crack from tips of strike-slip flaw. In: The 42nd US rock mechanics symposium (USRMS). American Rock Mechanics Association, pp 221–321

Yang S, Jing H (2011) Strength failure and crack coalescence behavior of brittle sandstone samples containing a single fissure under uniaxial compression. Int J Fract 168:227–250

Yang S, Jiang Y, Xu W, Chen X (2008) Experimental investigation on strength and failure behavior of pre-cracked marble under conventional triaxial compression. Int J Solids Struct 45:4796–4819

Yang S, Jing H, Wang S (2012) Experimental investigation on the strength, deformability, failure behavior and acoustic emission locations of red sandstone under triaxial compression. Rock Mech Rock Eng 45:583–606

Yang S, Liu X, Jing H (2013) Experimental investigation on fracture coalescence behavior of red sandstone containing two unparallel fissures under uniaxial compression. Int J Rock Mech Min 63:82–92. doi:10.1016/j.ijrmms.2013.06.008

Yin P, Wong RHC, Chau KT (2014) Coalescence of two parallel pre-existing surface cracks in granite. Int J Rock Mech Min 68:66–84